Iraqi Journal of Physics, 2026
https://doi.org/10.30723/ijp.v24i3.1371

Vol.24, No.3, PP.12-24
P-ISSN: 2070-4003
E-ISSN: 2664-5548

Effects of Manganese (Mn) Substitution on the Structural, Surface, and Magnetic Properties of $Zn_{1-X}Mn_xFe_2O_4$ Nanostructures Prepared by Hydrothermal

Nabaa A. Ibrahim[1*] and Suhad A. Hamdan[1]
[1]*Department of Physics, College of Science, University of Baghdad, Baghdad, Iraq*
[*]Corresponding author: naba.ahmed2304@sc.uobaghdad.edu.iq

Abstract

This study investigates the effects of manganese (Mn) substitution on the structural, surface, and magnetic properties of spinel ferrite ($Zn_{1-x}Mn_xFe_2O_4$) prepared by the hydrothermal method. X-ray diffraction (XRD) confirmed the spinel ferrite phase, with minor shifts in diffraction peaks due to variations in lattice parameters after Mn substitution. Field-emission scanning electron microscopy (FESEM) revealed spherical nanoparticles with average sizes ranging from 21 to 100 nm, varying with the Mn content. The vibrating sample magnetometry (VSM) demonstrated the highest saturation magnetization (M_s =17.35 emu/g) at x = 0.4, attributed to optimal Mn substitution that enhances superexchange interactions. However, excessive Mn concentration led to reduced magnetization. Additionally, the coercivity (H_c) increased slightly at x = 0.2 (Oe= 293) due to changes in anisotropy caused by particle size and shape variations. The results demonstrated how Mn substitution at a moderate ratio adjusted the surface morphology, magnetic, and structural characteristics of $Zn_{1-x}Mn_xFe_2O_4$, which makes them candidates for various applications.

Article Info.

Keywords:
Spinel Ferrite, Structural Properties, Magnetic Properties, FESEM, $Zn_{1-X}Mn_xFe_2O_4$.

Article history:
Received: Sep. 09, 2024
Revised: Feb. 22, 2025
Accepted:Mar. 02, 2025
Published:Sep. 01,2026

1. Introduction

Spinel ferrite is a well-known magnetic material with the chemical formula MFe_2O_4, where M represents one of the ions Zn^{2+}, Mn^{2+}, Co^{2+}, or Ni^{2+}. The spinel ferrite has a face-centered cubic (fcc) structure [1]. There are two types of sites within this structure: site A, which is occupied by divalent metal ions, and site B, which is occupied by iron ions (Fe^{3+}) in addition to oxygen ions [2,3]. The distribution of cations between the two sites determines the magnetic properties of the prepared samples. Researchers can precisely control cation distribution by optimizing the synthesis parameters, such as temperature, pH, and dopant concentration, enabling the tailored design of ferrites for specific magnetic and technological applications. In the inverse spinel, half of the trivalent metal ions are occupied in the tetrahedral sites, with the remaining trivalent metal ions and all divalent metal ions distributed in the octahedral sites [4].

Because of their unique magnetic and electrical characteristics, spinel ferrites are being researched extensively. They are used in various fields, such as biomedical applications, catalysts, chemical sensors, data storage devices, and magnetic resonance imaging (MRI) [5]. The cation distribution between the tetrahedral and octahedral sites inside the spinel structure and the bond lengths affect the material's physical characteristics, especially its magnetic characteristics [6]. The exchange interactions inside the crystal lattice are greatly improved by substituting ions with various magnetic moments. The redistribution of cations between the two sites as a result of this substitution directly impacts the magnetic properties [7].

Changing the bond angles and lattice dimensions of the spinel structure can be done by substituting metal ions with different ionic radii, which induces lattice distortions or strain, causing an increase in magnetization and intensifying magnetic coupling. The variations in the ion jump lengths impact saturation magnetization, coercivity, and Curie temperature through superexchange interactions, especially between Fe^{3+} ions between the A and B sites. Controlling substituted elements and their ratio can improve ferrite-based devices [8]. The size and level of aggregation of the nanoparticles in ferrite materials majorly impact their magnetic

characteristics. The material may display superparamagnetism through enhanced super-exchange interactions when the particle size falls below a threshold point [9]. The degree of aggregation between nanostructures influences the dipole-dipole interactions. Coercivity and remanence can both be enhanced by stronger contacts. Multi-domain behavior and a reduction in superparamagnetic effects are possible outcomes of aggregated nanoparticles acting as bigger particles [9,10].

Zhu et al. (2020) [11] synthesized $ZnFe_2O_4$ using hydrothermal and ceramic methods, comparing their structural and magnetic properties. The hydrothermal method resulted in higher magnetism due to Fe ion occupancy changes caused by Zn loss during the hydrothermal Process. Hangai et al. (2021) [12] developed the properties of $ZnFe_2O_4$ nanoparticles coated with poly-2-hydroxyethyl methacrylate (PHEMA) using microwave-assisted hydrothermal synthesis. The nanoparticles exhibited controlled magnetic properties and no cytotoxicity, making them promising for biomedical applications, like cancer therapy. Aubekerov et al. (2022) [13] created $ZnO/ZnFe_2O_4$ nanostructures for gas sensors by immersing ZnO nanowires in ferrous sulfate. Raman spectroscopy confirmed structural changes, and the materials showed enhanced sensitivity to isopropyl alcohol vapors. Faramawy and El-Sayed (2024) [14] synthesized a $CuFe_2O_4/ZnFe_2O$ core/shell nanostructure with increased magnetization and reduced photoluminescence. The findings suggested applications in high-frequency transformer cores and photocatalysis for water purification and hydrogen production. Mohammed and Hamdan (2024) [15] investigated the pH effects on $CoFe_2O_4$ nanostructures synthesized via hydrothermal methods. Magnetic and structural properties varied with pH, demonstrating ferromagnetic behavior and pH-dependent crystallite size changes

This study focuses on synthesizing high-purity spinel ferrite ($Zn_{1-x}Mn_xFe_2O_4$) nanostructures and explores the effect of the Mn substitution ratio on the structural and magnetic properties. Advanced characterization techniques, including X-ray Diffraction (XRD) analysis, field-emission scanning electron microscopy (FE-SEM), and Vibrating Sample Magnetometry (VSM), were employed to investigate these effects. Additionally, this study examines how changes in the ion jump length within the lattice affect the magnetic properties to estimate a relation between structural changes and magnetic behaviors.

2. Experimental Work

The $Zn_{1-x}Mn_xFe_2O_4$ was prepared from metal nitrates using the hydrothermal method. The metal nitrates ($Zn(NO_3)_2\cdot 6H_2O$, $Fe(NO_3)_3\cdot 9H_2O$, and $Mn(NO_3)_2$) at a 0.2 M concentration were separately dissolved in distilled water using a magnetic stirrer. 1 M NaOH was dissolved in deionized water at 70 °C with stirring until the solution showed a transparent appearance. Then, the metal salt solutions at their specific ratios were gradually added to the boiled NaOH solution. The pH of the solution was adjusted to 9 and stirred for 6 h at 70 °C until it turned black in color. The resulting solution was positioned in an autoclave at 100 °C for 3 h; then centrifuged for 30 min at 6000 rpm. The centrifugation was repeated three times. The resulting precipitate was dried at 100 °C for 30 min and ground to a black powder. The powder was calcined at 600 °C. The procedure was repeated at various Mn substitution ratios. Various characterization techniques were utilized to assess the samples, focusing on their structural and morphological properties using XRD analysis, FE-SEM, and VSM, which assessed the magnetic properties of the prepared samples.

3. Results and Discussions

3.1. X-ray Diffraction (XRD)

Fig. 1 shows the XRD patterns of $Zn_{1-x}Mn_xFe_2O_4$ samples prepared at different substitution ratios of Mn atoms (x= 0, 0.2, 0.4, 0.6, 0.8, and 1) using the hydrothermal technique. The polycrystalline structure for all patterns appeared with diffraction peaks at 2θ =

18.5287°, 30.2991°, 35.5880°, 37.0991°, 43.2598°, 53.5290°, 57.1429°, 62.7243°, 71.0874°, and 73.9796°, corresponding to standard diffracted lines matched with (111), (220), (311), (222), (400), (422), (511), (440), (620), and (533) crystalline planes, respectively, of the spinel ferrite structure. These diffraction lines match the JCPDS card 01-077-001-10860 lines for Spinel zinc ferrite. Additional minor peaks were noted in the patterns corresponding to the Hemetite structure (Fe_2O_3). These results agreed with those of Algarni et al. [8].

Increasing Mn substitution did not induce any phase changes in the samples, confirming the retention of the spinel ferrite structure. The replacement of Zn with Mn resulted in slight shifts of the diffraction peaks toward higher 2θ values, indicating a minor contraction in the lattice dimensions. The lattice parameter varied depending on the substituted cations, which made shifts in the diffraction patterns possible due to the variation in the ion radius of substituted Mn instead of Zn [r_{Mn} (0.8Å) > r_{Zn} (0.74Å)][16]. Crystallinity is reduced, in addition to increasing line broadening, indicating a reduction in crystallite size with increasing Mn substitution in the Zn ferrite sample. This result is in agreement with that of Tudorache et al. [17]. It is important to note that spinel ferrites MFe_2O_4 have very similar crystal structures, with some differences in their lattice parameters. Thus, they have similar XRD patterns with slight shifts in the diffraction angles [18,19]. Using the Bragg formula, the interplanar spacing values between crystal planes ($d_{(hkl)}$) were measured according to the diffraction angles.

Fig. 2 shows the variation in crystallite size with Mn content in $Zn_{1-x}Mn_xFe_2O_4$, which was determined using the Scherrer formula (Eq. (1)) corresponding to the preferred orientation (311) in the XRD patterns [17]:

$$D = \frac{0.94\lambda}{\beta\cos\theta} \quad \textbf{(1)}$$

where θ is the angle of the diffracted X-ray, λ is the X-ray wavelength, and β is the line broadening.

The crystallite sizes decreased to 18.0, 17.5, 14.1, 13.7, 12.9, and 8.2 nm with the increase of the Mn content of x = 0, 0.2, 0.4, 0.6, 0.8, and 1, respectively. At the same time, the crystallite size for each direction was calculated using the Scherrer formula with the full width at half maximum (FWHM) of the diffracted lines, as listed in Table 1.

According to Eq. (2), the lattice constant of a cubic structure in the spinel phase is [18]:

$$d_{(hkl)} = \frac{a}{\sqrt{h^2+k^2+l^2}} \quad \textbf{(2)}$$

The lattice parameter (*a*) was determined from the slope of the plot between the d_{hkl} spacing against $1/\sqrt{h^2+k^2+l^2}$, for $Zn_{1-x}Mn_xFe_2O_4$ at different Mn substitution ratios, as shown in Fig. 3. All lines exhibit excellent agreement between the proposed lines and the experimental $d_{(hkl)}$ values, as evidenced by the high R^2 values approaching unity. The slope values shown in the equation of lines in each figure represent the (*a*) values.

Fig. 4 shows the lattice constant (a) variation of cubic spinel structure $Zn_{1-x}Mn_xFe_2O_4$ with x. It is observed that the lattice constant seems nearly constant with increasing x from 0 to 0.4. In contrast, the lattice constant significantly increased with an increase in the Mn substitution ratio up to x=1, due to the effect of substituting larger cations.

As listed in Table 2, the lattice parameters of the prepared $Zn_{1-x}Mn_xFe_2O_4$ increased from 8.3343 Å to 8.4737 Å with increasing x from 0 to 1. All values agree with previously reported spinel zinc ferrite ZnFe2O4 lattice parameters around 8.4 Å [20].

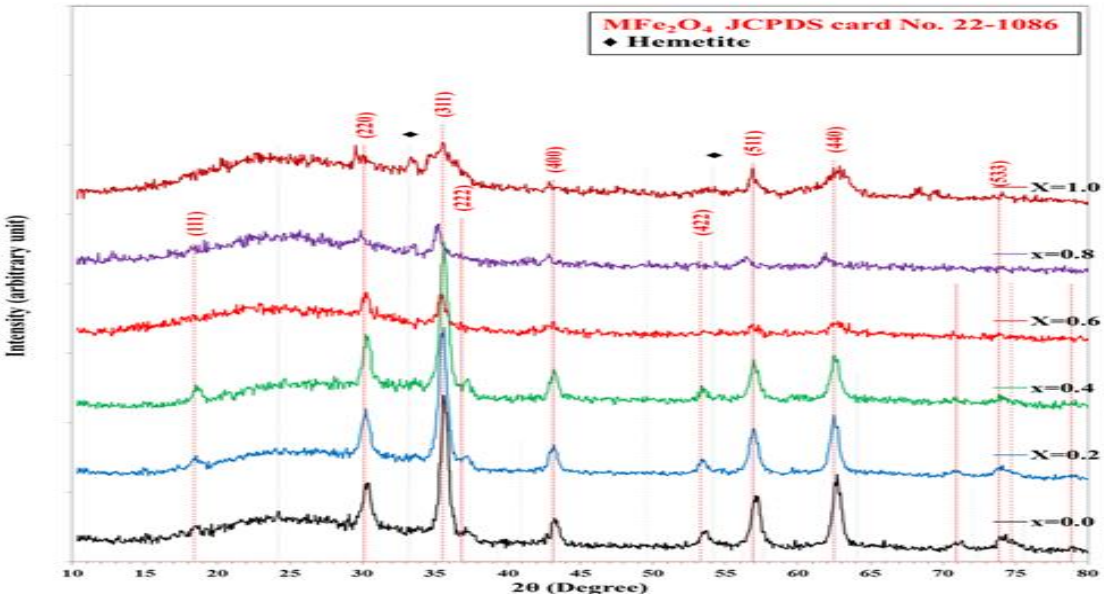

Figure 1: XRD patterns of $Zn_{1-x}Mn_xFe_2O_4$ samples prepared at different Mn substitutions.

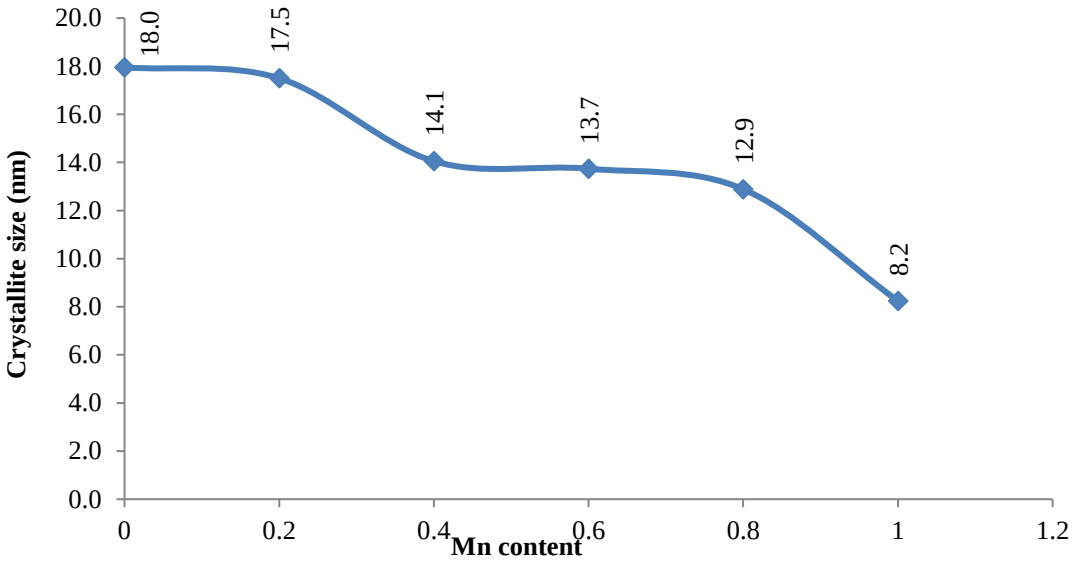

Figure 2: The change in crystallite size with Mn content in $Zn_{1-x}Mn_xFe_2O_4$.

The lattice density (ρ_x) of $Zn_{1-x}Mn_xFe_2O_4$ at different Mn substitution ratios was calculated using the Smith–Wijn formula [21]:

$$\rho_x = \frac{n\, M_w}{N_A\, a^3} \quad \textbf{(3)}$$

where N_A is Avogadro's number, n is the number of molecules per unit cell (n = 8 for spinel structure [21]), and M_w is the molecular weight, which is the summation of the ratio of each element multiplied by its atomic weight. The ion jump lengths at the tetrahedral site (L_A) and octahedral site (L_B) were calculated as follows [22]:

$$L_A = \frac{\sqrt{3}a}{4} \quad \textbf{(4)}$$

$$L_B = \frac{\sqrt{3}a}{2} \quad \textbf{(5)}$$

Table 1: XRD parameters of $Zn_{1-x}Mn_xFe_2O_4$ samples at different Mn substitutions.

x	2θ (Deg.)	FWHM (Deg.)	$d_{(hkl)}$ (Å)	C.S (nm)	(hkl)	Phase
0	18.5287	0.5785	4.7848	13.9	(111)	MFe_2O_4
	30.2991	0.7809	2.9475	10.5	(220)	MFe_2O_4
	35.5880	0.4650	2.5207	18.0	(311)	MFe_2O_4
	37.0991	0.7521	2.4214	11.1	(222)	MFe_2O_4
	43.2598	0.6652	2.0897	12.9	(400)	MFe_2O_4
	53.5290	0.6364	1.7105	14.0	(422)	MFe_2O_4
	57.1429	0.7520	1.6106	12.0	(511)	MFe_2O_4
	62.7243	0.7520	1.4801	12.4	(440)	MFe_2O_4
	71.0874	0.7810	1.3251	12.5	(620)	MFe_2O_4
	73.9796	0.8967	1.2803	11.1	(533)	MFe_2O_4
0.2	18.5508	0.6653	4.7791	12.1	(111)	MFe_2O_4
	30.2110	0.7232	2.9559	11.4	(220)	MFe_2O_4
	35.5581	0.4770	2.5227	17.5	(311)	MFe_2O_4
	37.1266	0.4918	2.4196	17.0	(222)	MFe_2O_4
	43.1426	0.6073	2.0951	14.1	(400)	MFe_2O_4
	53.3831	0.5786	1.7149	15.4	(422)	MFe_2O_4
	56.9393	0.6652	1.6159	13.6	(511)	MFe_2O_4
	62.4924	0.7232	1.4850	12.9	(440)	MFe_2O_4
	70.9126	0.6364	1.3279	15.3	(620)	MFe_2O_4
	73.9207	0.7521	1.2811	13.2	(533)	MFe_2O_4
0.4	18.4950	0.5785	4.7934	13.9	(111)	MFe_2O_4
	30.2941	0.6073	2.9480	13.6	(220)	MFe_2O_4
	35.5536	0.5940	2.5230	14.1	(311)	MFe_2O_4
	37.2095	0.4629	2.4144	18.1	(222)	MFe_2O_4
	43.1966	0.6652	2.0927	12.9	(400)	MFe_2O_4
	53.3794	0.5785	1.7150	15.4	(422)	MFe_2O_4
	56.9646	0.6074	1.6153	14.9	(511)	MFe_2O_4
	62.5182	0.6942	1.4845	13.4	(440)	MFe_2O_4
	70.8221	0.4050	1.3294	24.1	(620)	MFe_2O_4
	73.9459	0.6073	1.2808	16.4	(533)	MFe_2O_4
0.6	30.2339	0.5496	2.9537	15.0	(220)	MFe_2O_4
	35.4119	0.6073	2.5328	13.7	(311)	MFe_2O_4
	43.1363	0.6943	2.0954	12.3	(400)	MFe_2O_4
	56.8760	0.8967	1.6176	10.1	(511)	MFe_2O_4
	62.5454	1.0123	1.4839	9.2	(440)	MFe_2O_4
0.8	29.8836	0.5208	2.9875	15.8	(220)	MFe_2O_4
	35.1766	0.6470	2.5492	12.9	(311)	MFe_2O_4
	42.8435	0.5207	2.1091	16.4	(400)	MFe_2O_4
	56.4098	0.8100	1.6298	11.1	(511)	MFe_2O_4
	61.8766	0.8099	1.4983	11.4	(440)	MFe_2O_4
1	29.5322	0.4917	3.0223	16.7	(220)	MFe_2O_4
	35.4617	1.0125	2.5293	8.2	(311)	MFe_2O_4
	36.5029	0.3472	2.4595	24.1	(222)	MFe_2O_4
	56.8679	0.6075	1.6178	14.9	(511)	MFe_2O_4
	62.6821	1.0123	1.4810	9.2	(440)	MFe_2O_4

Table 2 lists the determined lattice constants (a), lattice volume (V), lattice density (ρ_x), and ion jump lengths L_A and L_B. The observed correlation between the ion jump lengths and the Mn substitution ratio in the $ZnFe_2O_4$ structure is due to differences in ionic radii [22]. The ion jump lengths increased with increasing Mn content.

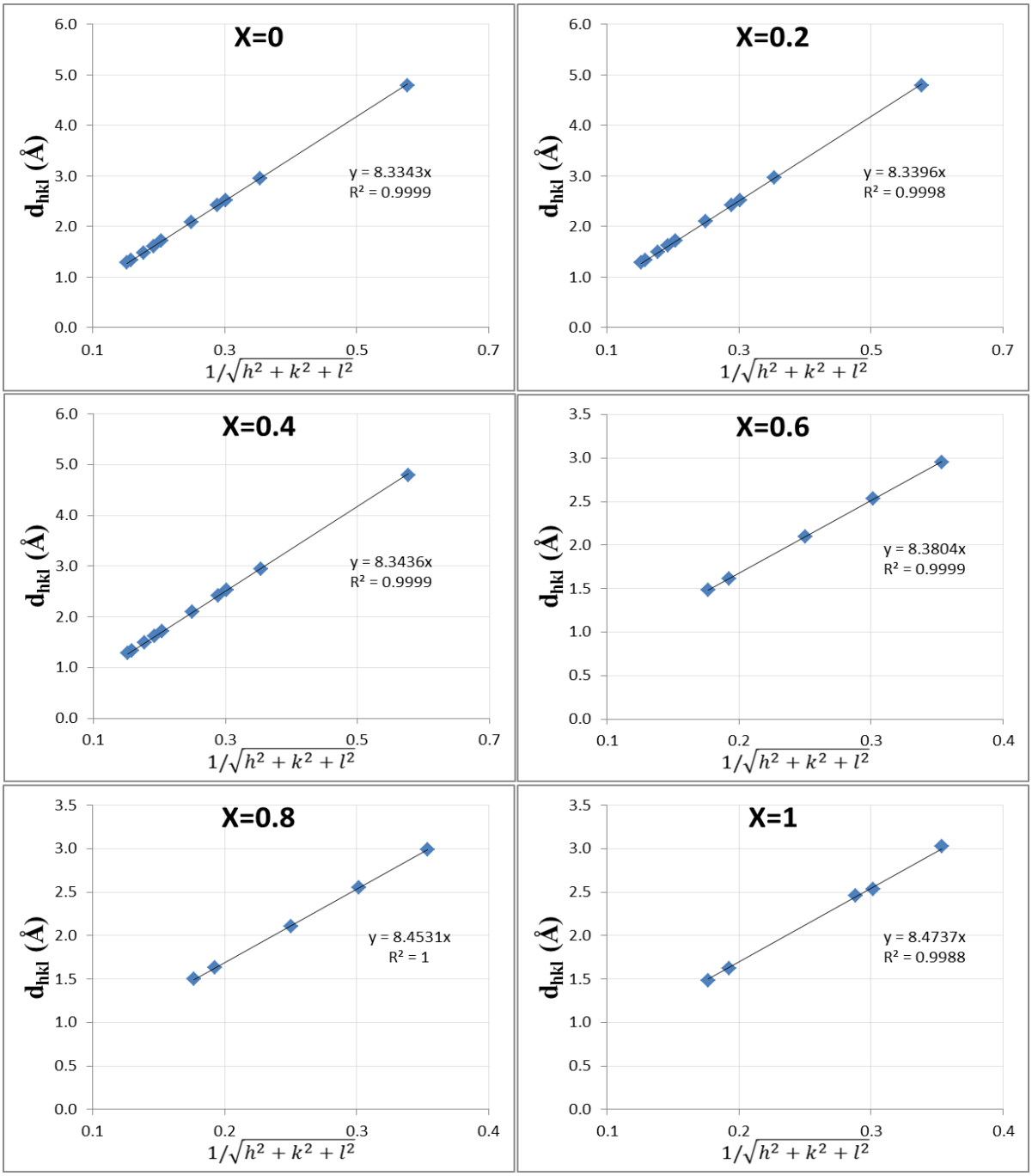

Figure 3: $d_{(hkl)}$ against $1/\sqrt{h^2+k^2+l^2}$ Plots for lattice constant determination for the cubic structure of $Zn_{1-x}Mn_xFe_2O_4$ at different Mn substitution ratios.

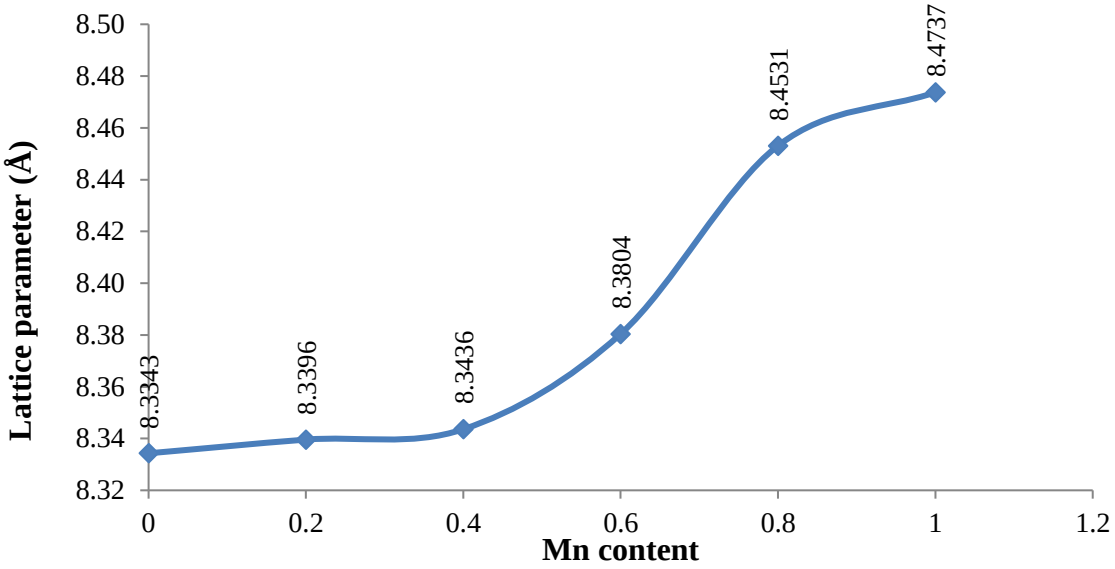

Figure 4: Lattice constant as a function of Mn content in $Zn_{1-x}Mn_xFe_2O_4$.

Table 2: lattice parameters (a), lattice volume (V), lattice density (ρ_x), and ion jump lengths (L_A, L_B) of spinel structure $Zn_{1-x}Mn_xFe_2O_4$ samples at different x.

X	*a* (Å)	V(Å^3)	ρ_x (g/cm^3)	L_A (Å)	L_B (Å)
0	8.3343	578.905	5.532	3.609	7.218
0.2	8.3396	580.010	5.474	3.611	7.222
0.4	8.3436	580.845	5.418	3.613	7.226
0.6	8.3804	588.565	5.300	3.629	7.258
0.8	8.4531	604.015	5.118	3.660	7.321
1	8.4737	608.442	5.036	3.669	7.338

3.2. Field Emission Scanning Electron Microscopy (FE-SEM)

Figs. 5 and 6 show the top-view FE-SEM images and particle size distributions of the surface nanoparticles of $Zn_{1-x}Mn_xFe_2O_4$ samples prepared at different substitution ratios of Mn (x= 0, 0.2, 0.4, 0.6, 0.8, and 1) using the hydrothermal technique. The surface morphology of the $ZnFe_2O_4$ sample (x=0) shows a structure of spherical particles aggregated with each other, forming a porous structure of uniform size across all samples. The histogram shows a uniform distribution with an average diameter of 63.9 nm and a standard deviation of particle size more significant than its average value of 27.0 nm. The incorporation of Mn into $Zn_{1-x}Mn_xFe_2O_4$ at different ratios significantly influences the particle size and distribution, affecting the magnetic properties. Specifically, at lower Mn substitution ratios (x = 0.2 and 0.4), the particles exhibit distinctive behaviors

At x = 0.2, the particles tended to aggregate more, indicating more interaction between particles. The increased aggregation may enhance magnetic interactions between particles, thus increasing magnetization. The average particle diameter was 21.0 nm. The size distribution was narrow, ranging from 12 to 32 nm. The low standard deviation of 4.2 nm suggests a uniform particle size distribution. At x = 0.4, the average particle diameter became 24.6 nm. The size distribution was narrower, ranging from 19 to 30 nm. The standard deviation was even lower at 2.5 nm, indicating an even more uniform particle size distribution, which is crucial for reproducible magnetic properties in practical applications. In addition, the sample porosity increased. Combining a small particle size and high porosity with an enhanced surface area could improve performance in applications, such as catalysis and biomedical imaging, where surface area and uniformity are critical [23].

The small particle size, narrow size distribution, and uniformity at these low Mn substitution ratios make the $Zn_{1-x}Mn_xFe_2O_4$ samples at x = 0.2 and x = 0.4 particularly interesting for applications requiring precise magnetic properties and high performance. These characteristics enhance the overall magnetic behavior, rendering them suitable for advanced technological applications [24].

Increasing the Mn substitution ratio to higher levels (x = 0.6, 0.8, and 1) in $Zn_{1-x}Mn_xFe_2O_4$ ferrite leads to an increase in the average particle size to 27.7, 45.25, and 100.5 nm and their standard deviations to 8.8, 30.1, and 73.1 nm, respectively, as illustrated in Table 3. Histograms for these samples show a wide and nonuniform distribution of particle sizes, indicating heterogeneity in particle formation. Highly merged nanoparticles at x = 1 can reduce the surface area and alter the magnetic interactions, contributing to the observed decrease in magnetization [25].

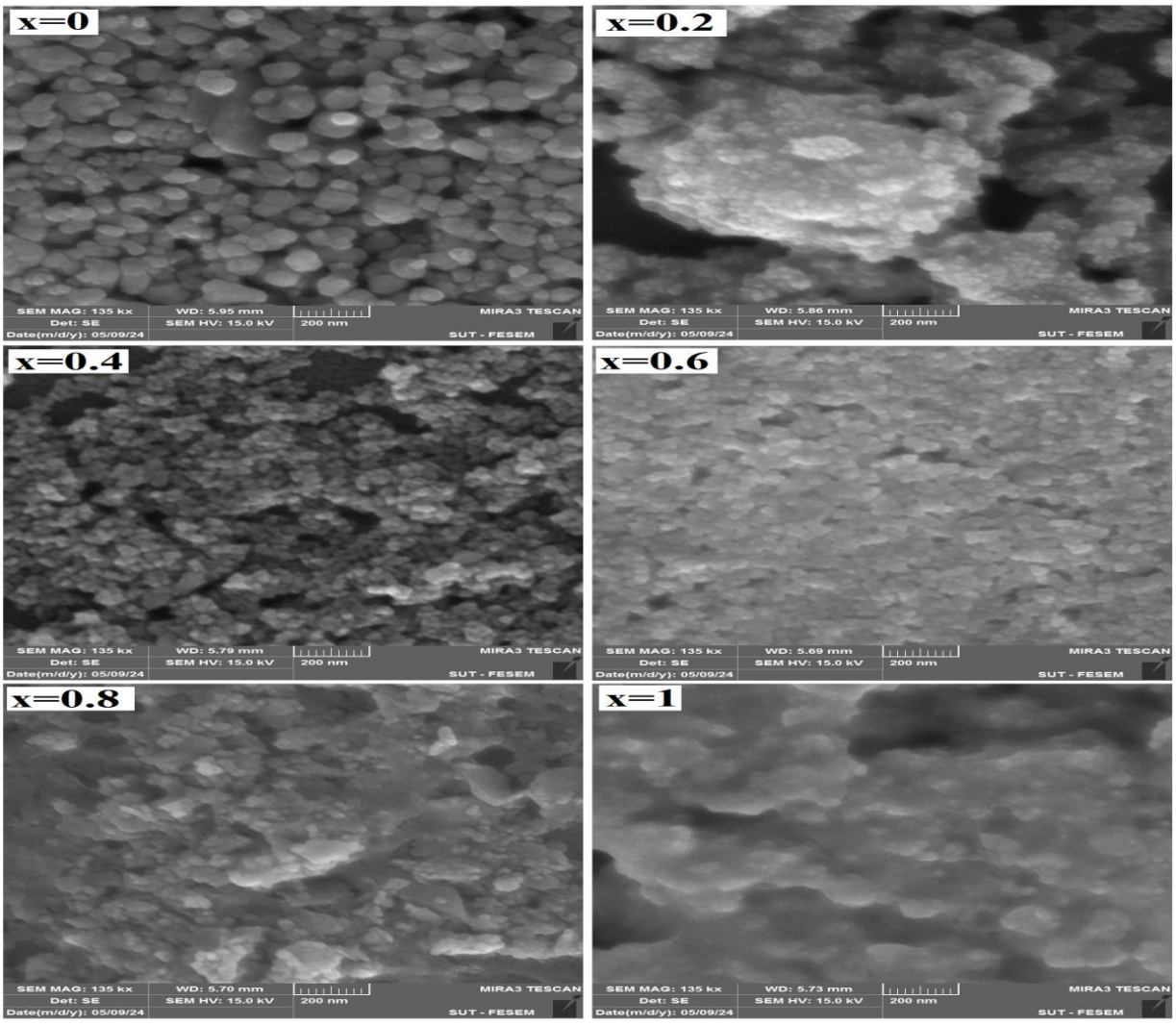

Figure 5: FE-SEM images of $Zn_{1-x}Mn_xFe_2O_4$ samples prepared by the hydrothermal method with different Mn substitutions.

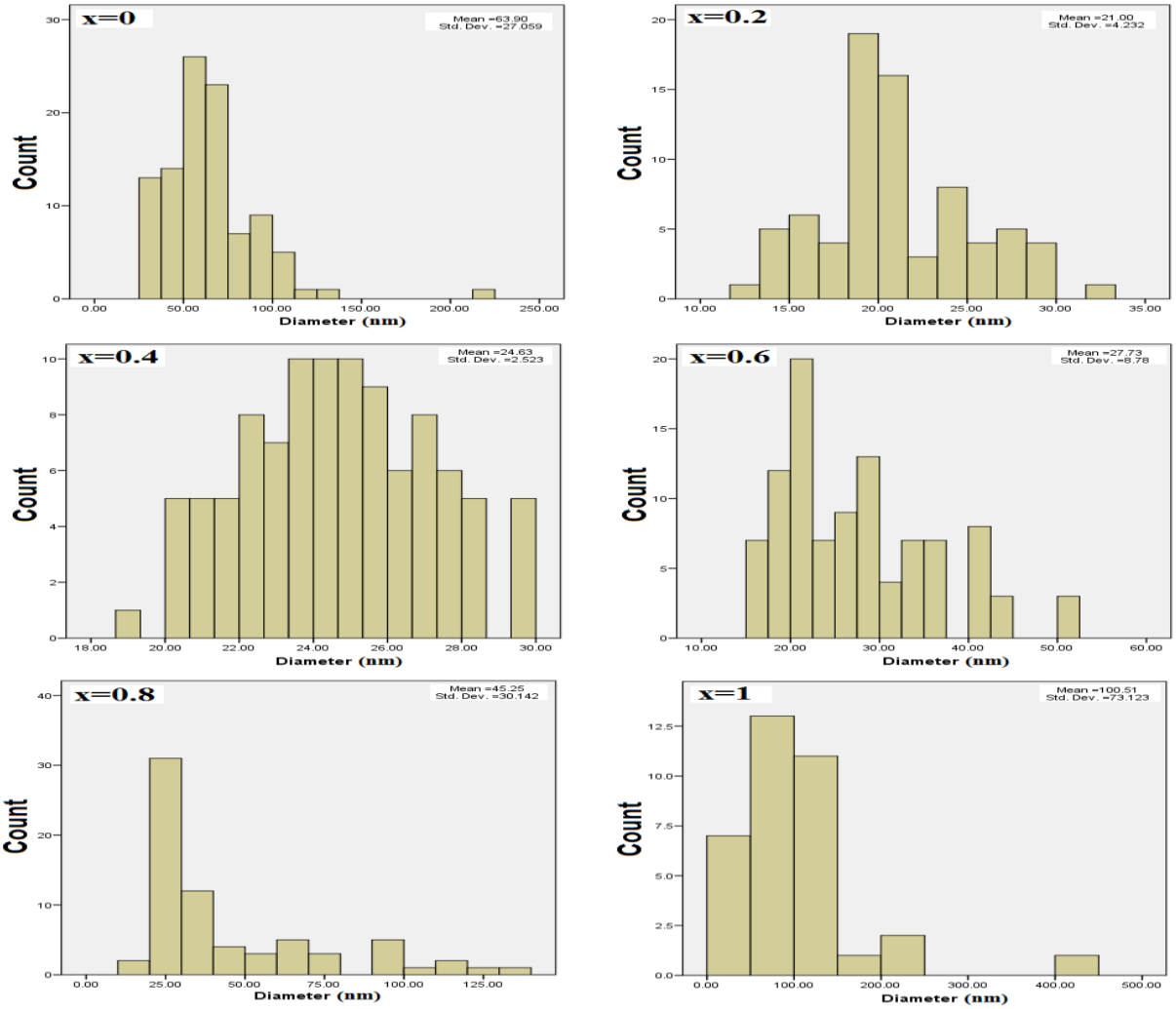

Figure 6: Particle size distribution of $Zn_{1-x}Mn_xFe_2O_4$ samples prepared by the hydrothermal method for different Mn substitutions (x=0, 0.2, 0.4, 0.6, 0.8, and 1).

Table 3: Average particle diameters and standard deviations from SEM images of $Zn_{1-x}Mn_xFe_2O_4$ samples prepared at different Mn substitutions.

x	Average diameter (nm)	Standard deviation (nm)
0	63.9	27.0
0.2	21.0	4.2
0.4	24.6	2.5
0.6	27.7	8.8
0.8	45.25	30.1
1	100.5	73.1

3.3. Magnetic Properties

The magnetic property test of $Zn_{1-x}Mn_xFe_2O_4$ samples prepared by a hydrothermal route at different Mn substitution ratios was examined using Vibrating Sample Magnetometry (VSM), as shown in Fig. 7. All samples exhibited a typical S-shaped hysteresis loop with a small area. With increasing Mn content, a noticeable variation in both residual magnetization (M_r) and coercive field (H_c) is observed. These changes indicate that Mn substitution alters the magnetic anisotropy and domain wall motion in the spinel structure.

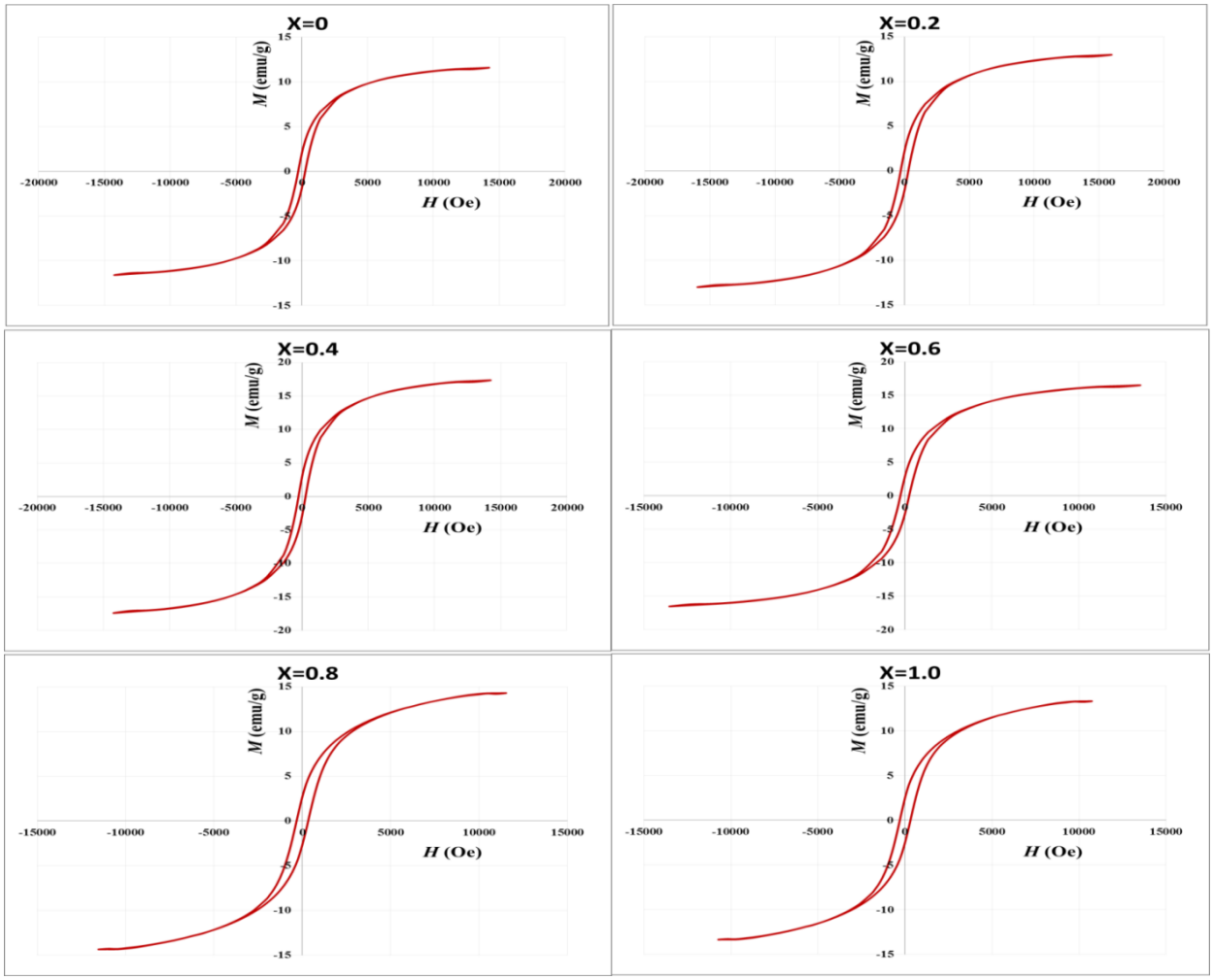

Figure 7: Magneto-hysteresis loop of $Zn_{1-x}Mn_xFe_2O_4$ samples prepared at different Mn substitutions.

Fig. 8 displays the variation in M_r and H_c of $Zn_{1-x}Mn_xFe_2O_4$ samples with x. The maximum M_r appeared at x = 0.4, whereas the maximum H_c appeared at x = 0.2. Both declined at higher Mn ratios.

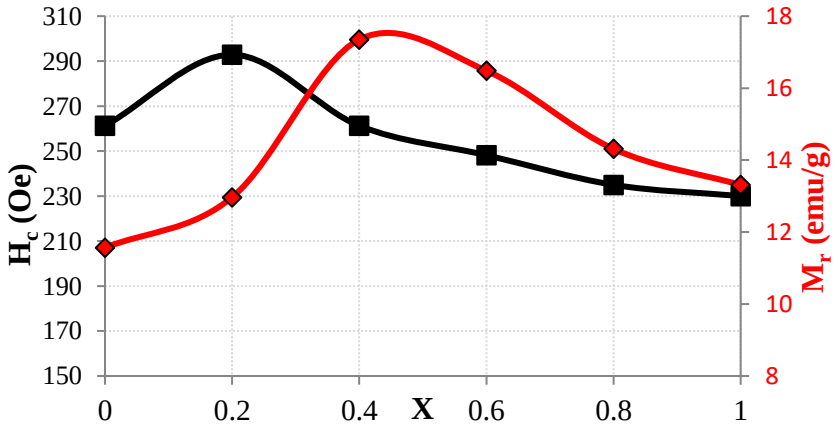

Figure 8: Variations in coercive field (H_c) and residual magnetization field (M_r) as a function of Mn substitution ratio of $Zn_{1-x}Mn_xFe_2O_4$ samples.

Table 4 lists the VSM parameters of the six metal ferrite samples. The highest value of saturation magnetization (M_s) of 17.35 emu/g was observed at x = 0.4. The increase in Mn substitution up to x = 0.4 enhances the magnetization, possibly due to the optimal replacement of Zn ions by Mn ions, which might increase the superexchange interactions between Fe^{3+} ions at the tetrahedral (A) and octahedral (B) sites. Beyond x = 0.4, the magnetization decreases, and excessive Mn substitution disrupts the balance of the magnetic interactions. M_r follows a trend similar to M_s, peaking at x = 0.4 and then decreasing, indicating stronger residual magnetization at intermediate Mn concentrations. The H_c slightly increased from 261 A/m at x = 0 to 293 A/m at x = 0.2 and then decreased as the Mn substitution increased. This indicates that moderate Mn substitution induces more anisotropy due to particle size and shape changes, but further substitution reduces this anisotropy.

The change in nanoparticle (NPs) size causes variations in physical and magnetic properties related to different mechanisms. For example, the physical radius of the NP, which determines its mobility and diffusion constant, may be smaller than the magnetic radius, which determines the effectiveness of the NP's magnetic moment. Clustering or agglomeration of nanoparticles emphasizes the importance of determining the particle radius. The particle size distribution also plays a vital role in accurately determining the magnetic moment of a particle [9].

Smaller particle sizes at intermediate Mn substitution ratios x = 0.2 might enhance the surface area, increasing superexchange interactions and magnetization. In addition, the variation in the ion jump length highly affects the magnetic properties [26]. Both L_A and L_B increase with increasing Mn substitution. Longer ion jump lengths at higher Mn concentrations may reduce the superexchange interaction efficiency, leading to decreased magnetization [26].

Table 4: Magnetization parameters of $Zn_{1-x}Mn_xFe_2O_4$ samples prepared at different Mn substitutions.

X	M_s (emu/g)	H_c (A/m)	M_r (emu/g)
0	11.57	261	2.0
0.2	12.97	293	2.2
0.4	17.35	261	2.9
0.6	16.48	248	2.8
0.8	14.31	235	2.7
1	13.31	230	2.5

4. Conclusions

In this work, $Zn_{1-x}MnxFe_2O_4$ nanostructures were successfully synthesized by the hydrothermal method at different Mn substitution ratios. XRD analysis confirmed the formation of the cubic spinel structure, with decreasing crystallite size and increasing lattice parameters and ion jump length as the Mn content increases. FE-SEM images showed that Mn substitution significantly affected particle size, distribution, and aggregation. The magnetic behaviour was strongly dependent on the Mn content, with the most favorable magnetic properties observed at an intermediate substitution ratio of x=0.4. Further Mn substitution reduced the magnetic performance because of changes in particle morphology and magnetic interactions. These findings demonstrate that controlling the Mn substitution ratio provides an effective approach for tuning the structural and magnetic properties of $Zn_{1-x}MnxFe_2O_4$ nanostructures.

Conflict of Interest

The authors declare no conflicts of interest.

References

1. T. Tatarchuk, M. Bououdina, J. Judith Vijaya, and L. John Kennedy, *in: Proceedings of the 4th International Conference Nanotechnology and Nanomaterials (NANO2016)*, 2017, edited by O. Fesenko and L. Yatsenko (Springer, 2017), p. 305. https://doi.org/10.1007/978-3-319-56422-7_22.
2. J. M. D. Coey. Magnetism and Magnetic Materials. 1st Ed. Cambridge: Cambridge University Press; 2010.
3. S. A. Luksic, B. J. Riley, M. Schweiger, and P. Hrma, Incorporating technetium in minerals and other solids: A review. *J. Nucl. Mater.* **466**, 526 (2015). https://doi.org/10.1016/j.jnucmat.2015.08.052.
4. S. Chikazumi and C. D. Graham Jr. Physics of Ferromagnetism. 2nd Ed. Oxford: Oxford University Press; 1997. http://dx.doi.org/10.1093/oso/9780198517764.001.0001.
5. Y. Oh, M. Sahu, S. Hajra, A. M. Padhan, S. Panda, and H. J. Kim, Spinel ferrites ($CoFe_2O_4$): synthesis, magnetic properties, and electromagnetic generator for vibration energy harvesting. *J. Electron. Mater.* **51**(5), 1933 (2022). https://doi.org/10.1007/s11664-022-09551-5.
6. Y. Zhang, Y. Chen, Q. Kou, Z. Wang, D. Han, Y. Sun, J. Yang, Y. Liu, and L. Yang, Effects of Nd concentration on structural and magnetic properties of $ZnFe_2O_4$ nanoparticles. *J. Mater. Sci. Mater. Electron*. **29**(5), 3665 (2018). https://doi.org/10.1007/s10854-017-8297-0.
7. Y. Sandeep, T. Rambabu, L. Kunja, O. Borang, G. Aravind, A. Dode, and V. Nathanial, Low sintering effect on structural, electrical and magnetic properties of rare-earth metal ion Er^{3+}-substituted nickel–zinc spinel ferrites. *J. Mater. Sci. Mater. Electron*. **33**(1), 635 (2022). https://doi.org/10.1007/s10854-021-07332-0.
8. T. S. Algarni, A. M. Al-Mohaimeed, A. B. Al-Odayni, and N. A. Y. Abduh, Activated carbon/$ZnFe_2O_4$ nanocomposite adsorbent for efficient removal of crystal violet cationic dye from aqueous solutions. *Nanomaterials.* **12**(18), 3224 (2022). https://doi.org/10.3390/nano12183224.
9. B. Issa, I. M. Obaidat, B. A. Albiss, and Y. Haik, Magnetic nanoparticles: surface effects and properties related to biomedicine applications. *Int. J. Mol. Sci*. **14**(11), 21266 (2013). https://doi.org/10.3390/ijms141121266.
10. S. A. Hamdan, Annealing Effect on Nickel Oxide Nanoparticles Properties, *Jordan J. Phys.* **16**(3), 373 (2023). https://doi.org/10.47011/16.3.12.
11. X. Zhu, C. Cao, S. Su, A. Xia, H. Zhang, H. Li, Z. Liu, and C. Jin, A comparative study of spinel $ZnFe_2O_4$ ferrites obtained via a hydrothermal and a ceramic route: Structural and magnetic properties, *Ceram. Int.* **47**(11), 15173 (2021). https://doi.org/10.1016/j.ceramint.2021.02.077.
12. B. Hangai, G. Acero, P. P. Ortega, F. G. Garcia, and A. Z. Simões, Bioactivity evaluation of nanosized $ZnFe_2O_4$ fabricated by hydrothermal method. *Process. Appl. Ceram.* **15**(4), 374 (2021). https://doi.org/10.2298/PAC2104374H.
13. K. Aubekerov, K. N. Punegova, R. Sergeenko, A. Kuznetsov, V. M. Kondratev, S. A. Kadinskaya, S. S. Nalimova, and V. A. Moshnikov, *in: Proceedings of the 23rd Russian Youth Conference on Physics of Semiconductors and Nanostructures, Opto- and Nanoelectronics (RYCPS 2021)*, 2022, edited by V. Moshnikov (St. Petersburg Polytechnic University, 2022), p. 012014. https://doi.org/10.1088/1742-6596/2227/1/012014.
14. A. M. Faramawy and H. M. El-Sayed, Enhancement of magnetization and optical properties of $CuFe_2O_4/ZnFe_2O_4$ core/shell nanostructure. *Sci. Rep.* **14**(1), 6935 (2024). https://doi.org/10.1038/s41598-024-57134-7.
15. A. J. Mohammed and S. A. Hamdan, The Influence of the Various pH values on structural and magnetic Properties of cobalt ferrite nanostructure. *Mustansiriyah J. Pure Appl. Sci.* **2**(1), 15 (2024). https://doi.org/10.47831/mjpas.v2i1.97.
16. L. Pauling, The Sizes of Ions and the Structure of Ionic Crystals. *J. Am. Chem. Soc.* **49**(3), 765 (1927). https://doi.org/10.1021/ja01402a019.
17. F. Tudorache, P. D. Popa, M. Dobromir, and F. Iacomi, Studies on the structure and gas sensing properties of nickel–cobalt ferrite thin films prepared by spin coating. *Mater. Sci. Eng. B.* **178**(20), 1334 (2013). https://doi.org/10.1016/j.mseb.2013.03.019.
18. K. Jalaiah, K. Chandra Mouli, K. Vijaya Babu, and R. V. Krishnaiah, Structural, electrical and magnetic properties of Mg-Zr co-substituted $Ni_{0.5}Zn_{0.5}Fe_2O_4$. *J. Sci. Adv. Mater. Devices* **4**(2), 310 (2019). https://doi.org/10.1016/j.jsamd.2018.12.004.
19. J. L. Ortiz-Quiñonez, U. Pal, and M. S. Villanueva, Structural, magnetic, and catalytic evaluation of spinel co, ni, and co–ni ferrite nanoparticles fabricated by low-temperature solution combustion process. *ACS Omega.* **3**(11), 14986 (2018). https://doi.org/10.1021/acsomega.8b02229.
20. J. P. Singh, R. C. Srivastava, H. M. Agrawal, and R. P. S. Kushwaha, ^{57}Fe Mössbauer spectroscopic study of nanostructured zinc ferrite. *Hyperfine Interact*. **183**(1), 221 (2008). https://doi.org/10.1007/s10751-008-9756-z.
21. A. R. Chavan, R. R. Chilwar, P. B. Kharat, and K. M. Jadhav, Effect of annealing temperature on structural, morphological, optical and magnetic properties of $NiFe_2O_4$ thin films. *J. Supercond. Nov. Magn.* **31**(9), 2949 (2018). https://doi.org/10.1007/s10948-018-4565-3.

22. R. Tiwari, M. De, H. S. Tewari, and S. K. Ghoshal, Structural and magnetic properties of tailored $NiFe_2O_4$ nanostructures synthesized using auto-combustion method. *Results Phys.* **16**, 102916 (2020). https://doi.org/10.1016/j.rinp.2019.102916.
23. S. R. Mokhosi, W. Mdlalose, A. Nhlapo, and M. Singh, Advances in the synthesis and application of magnetic ferrite nanoparticles for cancer therapy. *Pharmaceutics*. **14**(5), 937 (2022). https://doi.org/10.3390/pharmaceutics14050937.
24. A. G. Díez, M. Rincón-Iglesias, S. Lanceros-Méndez, J. Reguera, and E. Lizundia, Multicomponent magnetic nanoparticle engineering: the role of structure-property relationship in advanced applications. *Mater. Today Chem.* **26**, 101220 (2022). https://doi.org/10.1016/j.mtchem.2022.101220.
25. N. Yadav, A. Kumar, P. S. Rana, D. S. Rana, M. Arora, and R. P. Pant, Finite size effect on Sm^{3+} doped $Mn_{0.5}Zn_{0.5}Sm_xFe_{2-x}O_4$ ($0 \le x \le 0.5$) ferrite nanoparticles. *Ceram. Int.* **41**(7), 8623 (2015). https://doi.org/10.1016/j.ceramint.2015.03.072.
26. S. S. Phalake, M. S. Lad, K. V. Kadam, S. A. M. Tofail, N. D. Thorat, and V. M. Khot, Application of $Mn_xFe_{1-x}Fe_2O_4$ (x = 0-1) nanoparticles in magnetic fluid hyperthermia: correlation with cation distribution and magnetostructural properties. *ACS Omega.* **7**(51), 44187 (2022). https://doi.org/10.1021/acsomega.2c05651.

تأثير استبدال المنغنيزعلى الخصائص التركيبية والسطحية والمغناطيسية للهياكل النانوية $Zn_{1-x}MnxFe_2O_4$ المحضرة بالمعالجة الحرارية المائية

نبأ احمد ابراهيم[1] وسهاد عبدالكريم حمدان[1]
[1]قسم الفيزياء، كلية العلوم، جامعة بغداد، بغداد، العراق

الخلاصة

تبحث هذه الدراسة في تأثير استبدال المنغنيز (Mn) على الخصائص البنيوية والسطحية والمغناطيسية لفريت الإسبينيل ($Zn_{1-x}MnxFe_2O_4$) المُحضر بالطريقة الحرارية المائية. أكد حيود الأشعة السينية وجود طور فريت الإسبينيل، مع انزياحات طفيفة في قمم الحيود نتيجة لتغيرات في معلمات الشبكة البلورية بعد استبدال المنغنيز. كشف المجهر الإلكتروني الماسح ذو الانبعاث الميداني عن جسيمات نانوية كروية بأحجام متوسطة تتراوح بين 21 و100 نانومتر، وتختلف باختلاف محتوى المنغنيز. أظهر قياس المغناطيسية باستخدام عينة مهتزة أعلى قيمة للمغناطيسية التشبعية (17.35 وحدة كهرومغناطيسية/غرام) عند x = 0.4، ويعزى ذلك إلى الاستبدال الأمثل للمنغنيز الذي يعزز تفاعلات التبادل الفائق. مع ذلك، أدى التركيز الزائد للمنغنيز إلى انخفاض المغناطيسية. بالإضافة إلى ذلك، زادت قوة الإكراه المغناطيسي قليلاً عند (Oe = 293) x = 0.2 نتيجةً لتغيرات في الخواص المغناطيسية المتباينة الناجمة عن اختلافات حجم الجسيمات وشكلها. وقد أظهرت النتائج كيف أن استبدال المنغنيز بنسبة معتدلة قد عدّل مورفولوجيا السطح والخصائص المغناطيسية والبنيوية لمركب $Zn_{1-x}MnxFe_2O_4$، مما يجعله مرشحًا مناسبًا لتطبيقات متنوعة.

الكلمات المفتاحية: السبينيل فيرايت، تركيبي، مغناطيسي، المجهر الإلكتروني الماسح، فيريت الزنك والمنغنيز الإسبينلي.